Catch bond kinetics are instrumental to cohesion of fire ant rafts under load

Robert J. Wagner¹, Samuel C. Lamont¹, Zachary T. White¹, and Franck J. Vernerey^{*1}

¹ University of Colorado Boulder, USA

December 5, 2024

Abstract

Dynamic networks comprised of constituents that break and reform bonds reversibly are ubiquitous in nature owing to their modular architectures that enable functions like energy dissipation, self-healing, and even activity. While bond breaking depends only on the current configuration of attachment in these networks, reattachment depends also on the proximity of constituents. Therefore, macroscale dynamic networks (not benefited by the secondary interactions cohering their molecular analogs) must rely on primary bonds for cohesion and self-repair. Toward understanding how macroscale networks might adaptively achieve this, we explore the uniaxial tensile response of 2D rafts comprised of interlinked fire ants (S. invicta). Through experiments and discrete numerical modeling, we find that ant rafts adaptively stabilize their bonded ant-to-ant interactions in response to tensile strains, indicating catch bond dynamics. Consequently, low strain rates that should theoretically induce creep mechanics of these rafts instead induce elastic-like response. Our results suggest that this force-stabilization delays dissolution of the rafts and improves toughness. Nevertheless, above 35% strain low cohesion and biaxial stress states cause nucleation and growth of voids whose coalescence patterns result from forcestabilization. These voids mitigate structural repair until initial raft densities are restored and ants can reconnect across defects. However mechanical recovery of ant rafts during cyclic loading suggests that – even upon reinstatement of initial densities – ants exhibit slower repair kinetics if they were recently loaded at faster strain rates. These results exemplify fire ants' status as active agents capable of memory-driven, stimuli-response for potential inspiration of adaptive structural materials.

Dynamic bonds that detach and reform without damage are prerequisite to the spontaneous functionality and complex adaptive mechanics of living systems spanning from protein folding [12], mitosis [27], and tissue healing [2], to the reconfiguration of superorganismal networks [44, 13]. Two advantages imparted by such bonds and targeted by engineers in synthetic materials are improvements in toughness and the introduction of self-healing. These traits originate from dynamic bonds' abilities to dissociate from highly stretched states before reattaching into lower energy configurations. In this way, dynamic bonds avert rupture due to overstretching, dissipate energy, and allow networks to deform greatly without damage [42] 45, 17, 5. Yet, an often overlooked precondition of such bond exchange is that detached chains must remain in proximity with adjacent strands to reconnect [32]. This is naturally achieved by molecular-scale polymers whose inter-chain, secondary interactions (e.g., hydrogen bonding, Van der Waals forces, etc.) cohere tightly packed networks that heavily resist volumetric changes [8]. However, as inter-constituent length scales increase, such cohesive forces cannot sustain the network densities prerequisite for bond exchange and self-repair. Indeed, many networked structures of interest (e.g., swollen gels [48], 3], swarming robots 30, and latticed metamaterials 52) cannot rely on nanoscale interactions for cohesion. Instead, the bonds connecting each constituent in these networks must be designed to adaptively prevent mechanical degradation and subsequent network failure.

^{*}correspondence to: franck.vernerey@colorado.edu

One natural class of dynamic networks, from which we may gain insight into adaptive damage mitigation strategies, are condensed swarms of insects [13] and worms [7], which host visibly observable constituents and display complex stimuli-responses [36] [22] [49]. Exemplary amongst these are aggregations comprised of fire ants (S. invicta) [49], [46] that coalesce during floods [18] via the formation of physical ant-to-ant connections (e.g., leg-to-leg, leg-to-mandible, etc. [11]) hereafter referred to as bonds. This evolutionary propensity to grab onto one another for flood survival can be exploited to create ant aggregations, either by placing ants in water or perturbed confinement. Once formed, fire ant aggregations display intricate morphological and mechanical behaviors ranging from tower- [24], [21] and bridge-building [49], [46] to non-Newtonian [36], [43] and active [35] rheological response.

While the mechanical behavior of 3D ant aggregations has been fairly well studied [36] [43] [23], surprisingly little remains known about the dynamic bonding and emergent mechanics of planar ant rafts as they are predominantly found in nature [18] [49]. Indeed, when loaded in a rheometer, ants are forced to remain in close contact through spatial confinement, thus masking any influence of cohesion on mechanics [36] [43] [35]. Vertical, uniaxial tensile testing of 3D aggregations has produced valuable information about the efficacy of load sharing and provided estimates for peak ant bond rupture strength (~200 dynes) [23], but the 3D nature of these networks obfuscates visible damage traits and make detailed image analysis of defects in live aggregates difficult [11] [23] [24]. However, in water, ant rafts naturally assume roughly planar morphologies [1] [18] [49] [46] that lend themselves to 2D mechanical testing (Fig. [1]A-B), real-time visual observations, and network-scale biomimetic modeling. For these reasons, we here focus on the mechanical response of planar ant rafts. These planar networks are defined by a floating, structural layer of ants that adhere and transmit physical forces via dynamic, ant-to-ant bonds with a neighbor exchange rate (in unperturbed conditions) on the order of 10⁻²-10⁻³ s⁻¹ [49]. While a second, pedestrian layer of freely active ants walks atop the structural layer and mediates rafts' long-term morphogenesis [49], [46], we here focus on the ants comprising the structural layer, which govern short-term network topologies and mechanics.

First, to probe the rafts' rate-dependent responses, we loaded them in uniaxial tension to failure at variable strain rates, while measuring the reaction force to estimate raft-scale stress and conducting image analysis to characterize topological evolution. Results indicate that – prior to major damage onset – ant rafts behave more elastically under applied strain than they do in unperturbed conditions. This is suggestive of mechanosensitive catch bond kinetics, whereby bonds increase their characteristic lifetimes under some range of applied force [31], as seen in some molecular, biological systems [26, 31, 38, 33]. Despite this, some degree of rate-dependent mechanical response is preserved due to rafts' rates of conformational change, analogous to α -relaxation in polymers [28]. Given the weak cohesion between non-bonded ants (which are held together by weak capillary effects [15, 14]), rafts exhibit early nucleation and growth of voids that cannot heal during loading and whose growth/coalescence kinetics provide further evidence of catch bond behavior. To substantiate these experimental deductions, we utilize a full-scale, discrete network model that predicts characteristic stress and damage responses in alignment with experimental results. Finally, to better probe associative kinetics and self-healing characteristics, we cyclically loaded ant rafts twice to 50% strain with variable recovery times between cycles. Our results suggest that – as with 3D aggregations 23 - ant rafts returned to their initial densities are able to self-heal defects and recover mechanical strength through density-dependent association kinetics. Together, these effects culminate in a material that is effectively a transient network when at rest, but elastic under load.

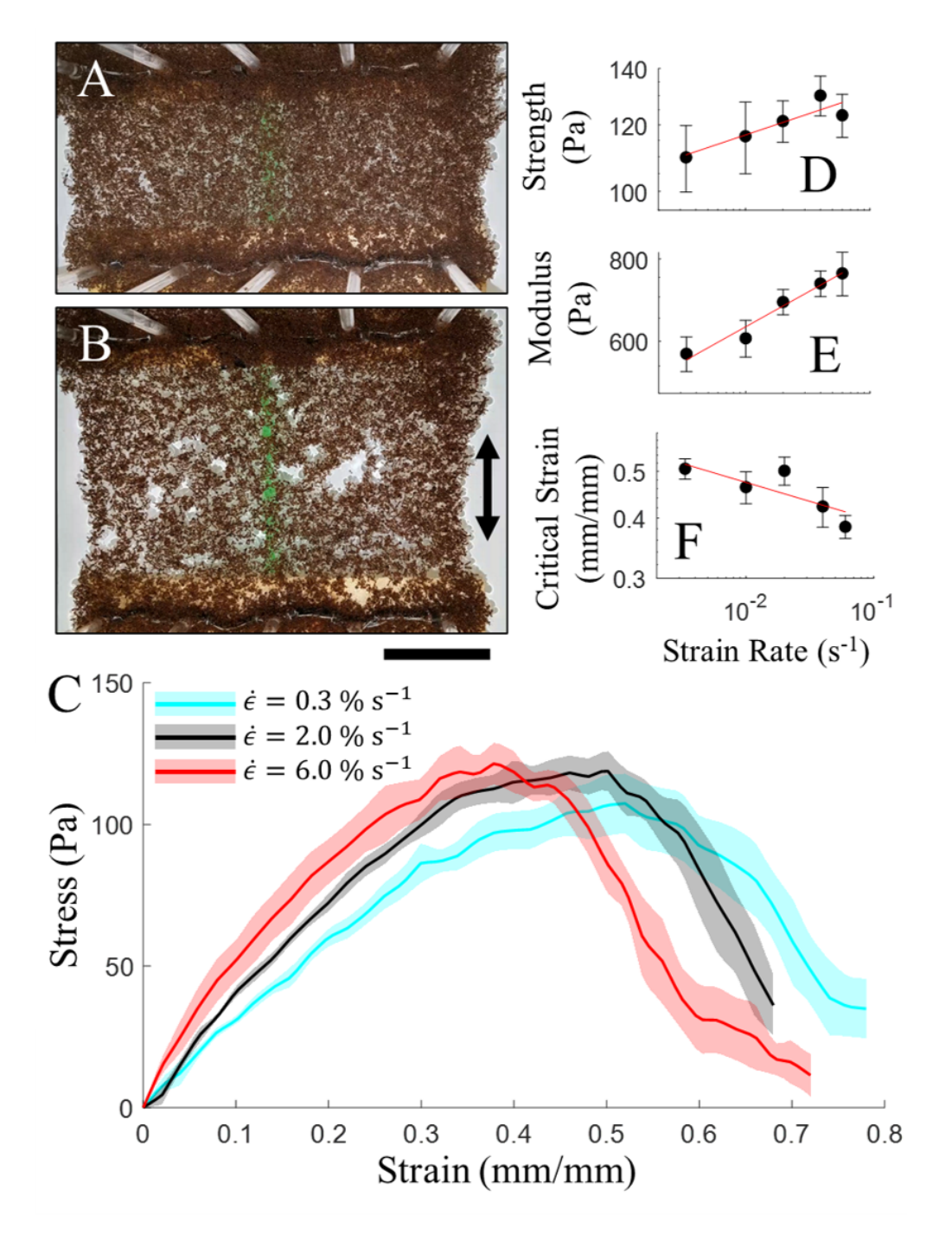


Figure 1: **(A-B)** Top views of an ant raft undergoing uniaxial tension at **(A)** 0% and **(B)** 50% strain. The two-headed arrow in **(B)** denotes the loading direction. The scale bar represents 20 ℓ where 1 ℓ = 2.93 mm is the measured average body length of an ant. **(C)** Ensemble-averaged (n=4) engineering stress versus strain for ant rafts loaded at strain rates of $\dot{\epsilon} = 0.3\%$ Hz (cyan), $\dot{\epsilon} = 2\%$ Hz (black), and $\dot{\epsilon} = 6\%$ Hz (red). See Figs. S5-S6 for the extended stress data. Shaded regions represent standard error of the mean (S.E.). **(D-F)** Ensemble-averaged (n=4) values of **(D)** ultimate strength (taken as the peak engineering stress), **(E)** small strain Young's modulus (taken as the average tangent of stress-strain up to 10% strain), and **(F)** critical engineering strain (taken at peak stress) with respect to strain rate.

Mechanical response suggests force-stabilizing bonds

Provided clear evidence of dynamic bonding in ant structures from prior work [36] [23] [43] [49] [46], we hypothesized that reversible bond exchange would allow ant rafts to undergo close-to steady-state creep when loaded at slow strain rates (relative to their unperturbed or nominal bond dissociation rate, \bar{k}_d^0 – see **Methods and Materials** and Fig. S1 for details of estimation) while displaying increasingly elastic behavior at higher relative loading rates. To test this hypothesis, we loaded rafts under uniaxial tension to failure at strain rates of $\dot{\epsilon} = \{0.3, 1, 2, 4, 6\}\%$ s⁻¹ (see Fig. [1]A and Movies S1-S3). Each raft was initially 100 mm × 200 mm (in the loading × transverse directions) and contained on the order 6,000 ants (see the **Materials and Methods** and Figs. S2-S4 for experimental setup details).

Our results indicate that ant rafts are very soft structures with peak stresses on the order of just 100 Pa (Fig. \square C-D). Nevertheless, their ensemble average (n=4) stress response (Fig. \square C), indicates that rafts exhibit measurable rate-dependence prior to major damage onset, whereby higher strain rates produce higher peak stresses (Fig. \square D) and initial tangent Young's moduli (Fig. \square E), but lower critical strains (Fig. \square F). However, decreased stiffness at lower strain rates offsets the slight gains in extensibility so that there is no statistically significant correlation between mechanical toughness and the applied loading rate (Fig. S5.D). This rate-dependent response is reminiscent of both biological \square 9 and synthetic \square 50 dynamically bonded polymers, albeit far less pronounced.

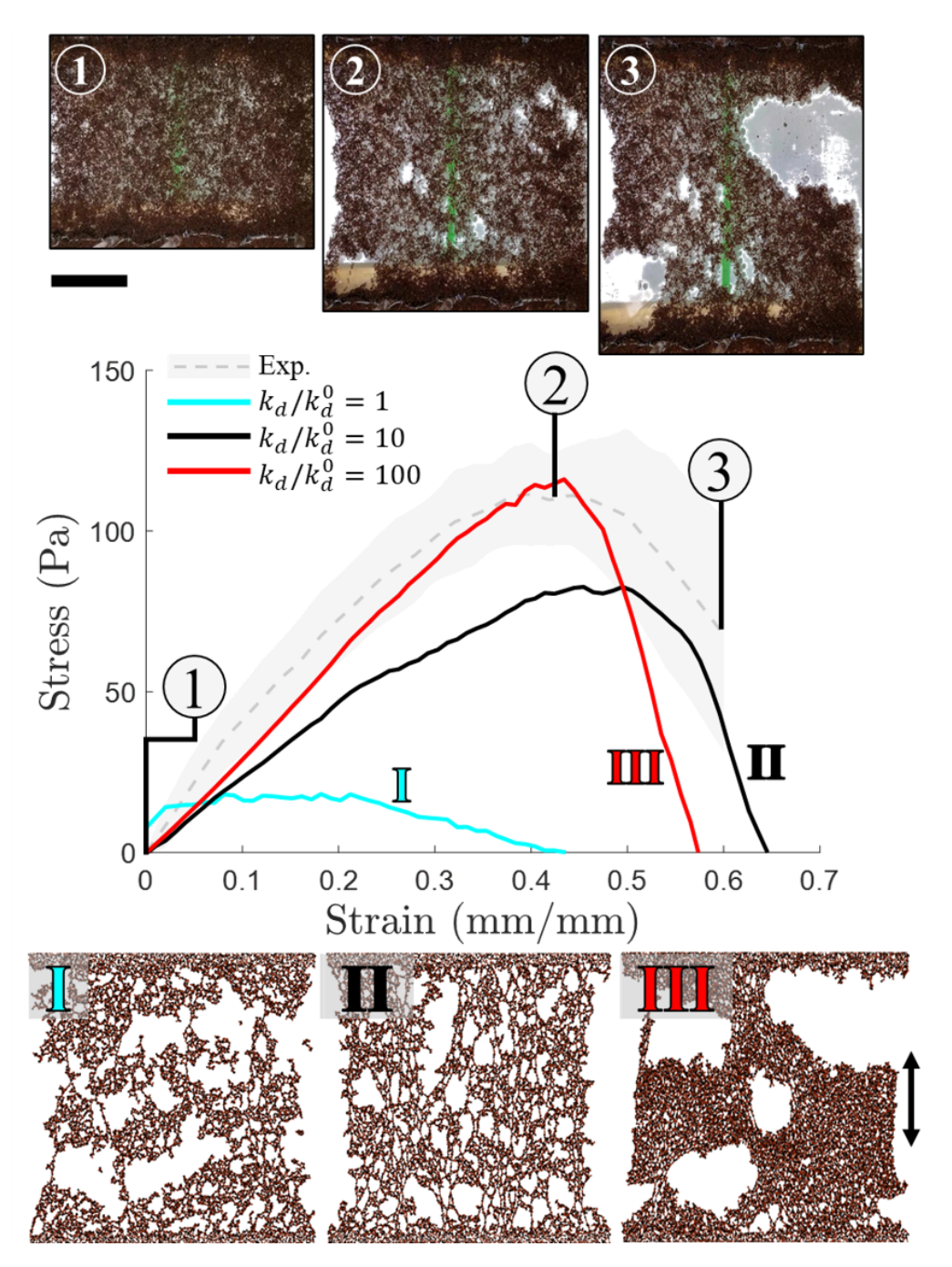


Figure 2: Engineering stress-strain response is shown, as predicted by the numerical model when $k_d/\bar{k}_d^0=1$ (cyan), $k_d/\bar{k}_d^0=1/10$ (black), and $k_d/\bar{k}_d^0=1/100$ (red), where \bar{k}_d^0 is the average detachment rate measured in unperturbed ant rafts (Fig. S1.A). The ensemble average (n=20) of all experimental stress-strain data is plotted as a grey dashed curve with the shaded region representing one standard deviation. Snapshots of the numerical rafts at 60% strain for (I) $k_d/\bar{k}_d^0=1$, (II) $k_d/\bar{k}_d^0=1/10$, and (III) $k_d/\bar{k}_d^0=1/100$ are shown. For reference, an experimental raft is shown at strains of roughly (1) 0%, (2) 40%, and – for direct comparison with numerical results – (3) 60% strain. The scale bar in the top left represents 20ℓ and is common to both experimental photos and simulated snapshots.

The rate-dependent mechanics of biological swarms are demonstrably driven by multiple characteristic time scales $\boxed{19}$. The network reconfiguration time scale, τ_{net} , (often taken as $1/\bar{k}_d^0$ in the context of transient networks $\boxed{42}$, $\boxed{45}$) is associated with topological rearrangement such as bond dissociation and neighbor exchange. Meanwhile, conformational relaxation time scales, τ_{relax} , derive from strain localization

and constituent re-alignment due to effects such as viscous drag, friction between neighboring constituents, and intrinsic bond relaxation. When dynamic networks are loaded at strain rates with characteristic times, $\tau_{strain} = 1/\dot{\epsilon}$, larger than $2\tau_{net}$, their ability to reconfigure during loading often allows them to creep and withstand strains on the order of 1,000% without damage [5, 10, 39, 50]. In contrast, when $\tau_{strain} << 2\tau_{net}$, the networks' configurations remain relatively fixed during deformation so that rate-dependence originates solely from conformational timescales, culminating in a more elastic-like response. Our results suggest that under the prescribed loading conditions, the ant rafts fall into the latter category, as they experience rupture at peak strains near 80%, with no significant improvement in toughness at slower strain rates. Thus, rate-dependence appears dominated by non-affine conformational changes, which are detectable using particle image velocimetry (PIV) (see Materials and Methods, Figs. S7-S15, and Movies S4-S6 for details). However, to corroborate this notion we additionally employ a full-scale, discrete network model in which every ant is modeled as a rigid body connected by dynamic bonds of prescribed force-extension and kinetic attachment/detachment rates (Movie S7).

Our model allows us to precisely control bond-level properties within simulated networks, thus elucidating what traits are needed to reproduce the observed mechanical/topological responses. For details on the model implementation, see the **Methods and Materials**. The stress-strain response predicted by the model is depicted in Fig. 2 when the numerical detachment rate was set to \bar{k}_d^0 , $\bar{k}_d^0/10$, and $\bar{k}_d^0/100$, where $\bar{k}_d^0 \approx 7.4$ mHz is the experimentally measured dissociation rate in unperturbed rafts. A loading rate of $\dot{\epsilon} = 2\%$ s⁻¹ was applied. These predictions are plotted alongside the ensemble average of all experimental data in Fig. 2. Significantly, the predicted stress response most closely matches that of experiments when the numerical attachment rate is set two orders of magnitude lower than \bar{k}_d^0 , so that the characteristic timescale of network relaxation is significantly higher than that of loading (i.e., $\tau_{net}/\tau_{strain} \approx \dot{\epsilon}/k_d \approx 270$) and the networks are effectively elastic. Importantly, comparing the stress responses of the system prescribed with the fastest detachment rate (cyan curve in Fig. 2) to those of the systems hosting force-stabilized bonds (black and red curves in Fig. 2) reveals that force-stabilization substantially increases the strength and toughness of these networks.

It is further evident that without effectively elastic bonds, the topological damage patterns predicted by simulations (Fig. 2I-III) do not match those of experiments (Fig. 2I-3), as quantified and discussed further in the following section. We speculate that in the regime of loading rates and strains studied here, ants prevent an early dissolution of the raft (as shown in Fig. 2I) by tightening their hold on neighbors and thus maintaining connections for longer times, synonymous with catch bond kinetics. This is consistent with the findings of Phonekeo, et al. (2017) 23 who vertically loaded 3D assemblages of fire ants and reproduced their experimental observations with a dissociating lattice model presuming catch bond kinetics a priori 31. Based on this prolonging of perturbed bond lifetime, we expect that ant bonds in stretched rafts detach primarily due to over-stretching rather than stochastic dissociation, which should be expressed in their characteristic damage responses.

Damage signatures indicate weak cohesion and strain-driven bond failure

Despite minor, but measurable ant-to-ant cohesion through capillary effects [15] [14], fire ant rafts' topologies during loading are dominated by the nucleation, growth, and coalescence of voids (Fig. 2]1-3). Here, voids are defined as continuous, enclosed regions absent of ants whose characteristic sizes exceed the approximate areal envelopment, $A_r = \pi \ell^2$, of an ant with body length ℓ , and which therefore cannot be closed by ants reaching across them. We here conduct image analysis on experimental and simulated rafts to leverage these features for further insight into bonds' dissociative characteristics. Specifically, we compute the rafts' average void areas, A_v , and numbers of voids, N_v (see Materials and Methods, Figs. S16-S19, and Movies S8-S10 for details). Using our numerical model, we swept a two-dimensional parametric space describing the bond-level force-displacement relationship (see Materials and Methods for details). Fig. 3A presents the stress, void count, and average void area (normalized by A_r) for the ensemble average of all experiments (black). Results are also presented from the simulations (red) that expressed minimum

absolute error with respect to experimental data.

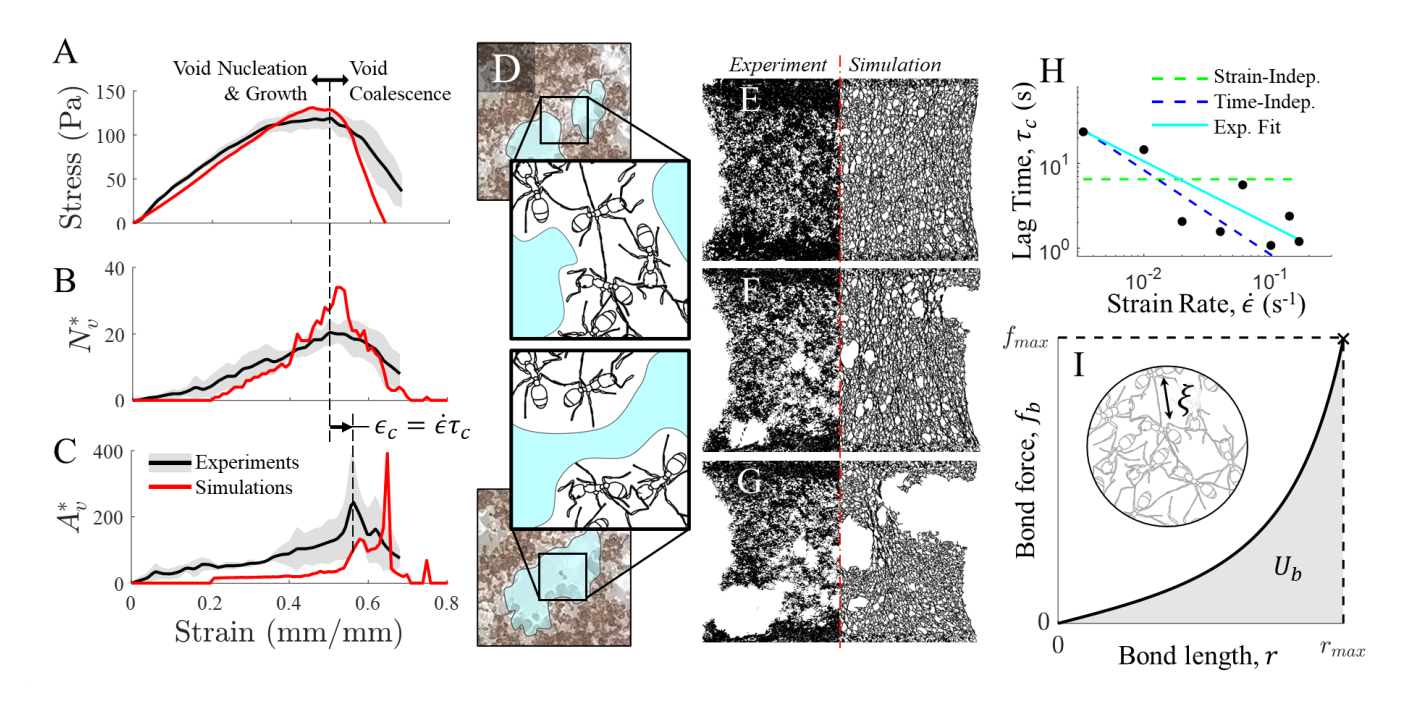


Figure 3: (A) Stress, (B) void count, N_v , and (C) average void area, A_v (normalized by the areal ant reach, A_r) plotted with respect to strain as measured from the ensemble average (n=20) of all experiments (black) and the simulation (red) with the lowest absolute error relative to experimental results. (D) An example of an experimental raft supplemented by illustrative diagrams before (top) and after (bottom) a filament of ants, which was separating two distinct voids (shaded blue), dissociates causing void coalescence. The photos in the background display the real rafts, while the illustrations in visually clarify the mechanism. (E-G) Binary snapshots of experimental (left) and simulated (right) ant rafts at (E) 15%, (F) 35%, and (G) 55% strain highlight topological similarities in void nucleation and coalescence patterns between model and experiments. Simulated rafts were treated elastically such that bond rupture only occurred at prescribed finite strain (i.e., $k_d/\bar{k}_d^0 \ll 1$) based on catch bond evidence. (H) Coalescence lag time, τ_c , with respect to strain rate, $\dot{\epsilon}$, for the experimentally measured data (black circles) and the experimental fit to said data using least-squares regression. I The bond force, f_b versus length, r_c , relation fitted from the discrete model, may be integrated to compute the single-bond energy at rupture as $U_b = \int f_b dr$ over the interval $r \in [0, r_{max}]$ where r_{max} is bond length at break. The inset displays an illustration of a fire ant network with characteristic mesh size, $\xi = \rho^{-0.5}$.

Neither the number of voids nor ensemble-averaged void area vary reliably with loading rate (Figs. S16-S17). However, these measures – along with stress – evolve non-monotonically and divulge that rafts undergo two distinct deformation regimes: a stiffening regime in which voids nucleate and grow, and a softening regime (after peak stress) in which voids rapidly coalesce (Fig. 3A-C). Before peak stress, numbers and areas of voids – although insensitive to loading rate – steadily increase with strain (Fig. 3B-C). However, in the softening regime, we observe a sharp increase in void area coinciding with a drop in void number. The sudden increase in void area is indicative of void coalescence, which occurs when ligaments that partition voids rupture (Fig. 3D). Figs. 3E-G depict snapshots of an experimental (left) and simulated (right) ant raft at the pre-localization (top), void nucleation and growth (center), and void coalescence (bottom) phases, respectively.

Since defect nucleation evidently precedes coalescence, a characteristic lag strain, ϵ_c , between these two phenomena may be measured and used to define a corresponding lag time, τ_c (Fig. 3B-C). This lag provides insight into the time- and stretch-dependence of local dissociation events. Having observed

that void coalescence is driven by the failure of inter-void ligaments (Fig. 3D), the lag strain may either depend on (a) the strain-dependent (and time-independent) rupture of ant-to-ant connections due to over-stretching, (b) the time-dependent (and strain-independent) stochastic detachment of these connections (at rate \bar{k}_d), or some combination. If the dissociative lag depends only on bond stretch, then the lag strain should be roughly constant, regardless of loading rate, so that $\tau_c \propto \dot{\epsilon}^{-1}$ (Fig. 3H, dashed blue line). On the other hand, if the lag strain depends only on the elapsed time because it is governed entirely by stochastic, strain-independent bond dissociation, τ_c should remain constant (Fig. 3H, dashed green line).

The experimental lag strain was computed as the strain at which peak cross-correlation between the number of voids and average void area occurs (see Methods and Materials, (9)). The resulting experimental data (Fig. 3H) reveals that $\tau_c \propto \dot{\epsilon}^{-0.75}$ ($R^2 = 0.90$), suggesting that void coalescence is mainly mediated by strain (i.e., bond stretch), rather than elapsed time (i.e., stochastic dissociation at the rate \bar{k}_d). This indicates that the merging of voids due to bond fracture is primarily driven by the finite extensibility of connections and that the bond lifetime plays a lesser role, providing further evidence of force-stabilizing catch bonds. Notably, as with stress responses, damage responses of experiments were not reproduced by simulated networks with large, finite detachment rates and instead k_d was set to $k_d \to 0$. Regardless, the network-scale patterns that these elastic dissociation events induce are reminiscent of those seen in most ductile materials, which usually exhibit high toughness, but low strength.

To establish a base-line toughness prediction, we consider a perfect network architecture akin to the classical Lake-Thomas model [16] [51], which posits that the toughness of a material is proportionate to its mesh size ξ , its concentration of load-carrying constituents c, and the energy, U_b , stored in a single unit at rupture (Fig. [31]). Having previously measured the planar density of rafts ($\rho = 0.304$ ants mm⁻²) [49], we take the mesh size, ξ , of our network to be $\xi \approx \rho^{-1/2} = 1.8$ mm, and determine $U_b = 1.275 \times 10^{-6}$ J based on the optimized force-extension relation predicted by the discrete model (see Materials and Methods), which yields a predicted toughness of roughly 1.96 Pa. As expected, the measured toughness values (Fig. S5.D) are greater than this quantity (by an order of magnitude), indicating that ant rafts are a ductile material. This relatively large toughness is however offset by a relatively low strength compared to molecular networks [5], [50], [17]. Using the experimentally calculated maximum force of ~ 200 dynes [23] and our fitted parameters from the simulations, the perfect network model predicts an ultimate strength of roughly 3.1 kPa, which is an order of magnitude larger than what we have observed experimentally.

Compared to polymer networks, the origins of concurrently low (albeit, higher than predicted) toughness and strength of ant rafts likely result from the lack of two important physical mechanisms. First, rather than resembling long polymer chains, ants have a small aspect ratio ($\sim 4:1$ [40]) so that they are not prone to the uncoiling and reptative disentanglement [28] that toughen polymers [41] [6]. Second, the cohesive force between ants is not strong enough to conserve raft areas. In contrast, high molecular cohesion in polymers [4] compels their chains to remain in close proximity, therefore limiting non-affine deformation and defect nucleation. This effect is amplified in dynamic polymers, where near-incompressibility conserves the concentration of open binding sites and therefore rates of bond attachment [32] [47].

Although ant rafts demonstrably cohere by surface tension [15], which may be sufficient to preserve the raft integrity at small strains/stresses the voids that emerge upon further loading appear to act as stress risers, imparting surrounding bond rupture and void growth that contrasts what occurs in polymers at moderate strains. Defect onset likely relies on two factors: first, the density and size of original defects in the network and, second, the imposition of biaxial stress. The latter is particular to the boundary conditions here and can be deduced from the propensity of void nucleation near the top and bottom boundaries (particularly at higher strains), where the raft cannot contract in the horizontal direction and thus experiences larger biaxial stresses.

As in most ductile materials [34], these voids do not merge in early stages, instead forming independently within the vicinity of one another. However, the transition to the softening region then occurs when merging of voids (via ligament rupture like that depicted in Fig. 3D) becomes the dominant mechanism, culminating with the stochastic formation of a macro-crack around 55% strain that causes the rest of the domain to experience elastic unloading and void closure. Regardless of deformation phase, the voids within

these macroscopic networks locally diminish the number of open binding sites available to constituents for reattachment and repair, especially around the damaged regions in which it is needed to sustain network integrity. However, this effect only persist without restoration of initial network densities.

Rafts' self-healing evinces strain-rate memory

Perhaps one of the most attractive features of dynamic networks is their capacity to heal damage through associative bond kinetics. While the damage analysis of the previous section provided insight into the conditions of dissociative kinetics in ant rafts, bond attachment events were hampered by a reduction in raft density. Therefore, to gauge the associative kinetic of fire ant rafts, we cyclically loaded them twice to 50% strain at two different strain rates, $\dot{\epsilon} = \{2,4\}s^{-1}$, and with five different hold times, $t_h = \{0,10,30,60,300\}s$, between cycles. Comparing the mechanical stress responses from cycle 2 to those of cycle 1 for the extreme hold times of 0 and 300 s (Fig. 4A-B), it is clear that the longer hold time permits better mechanical recovery, suggesting a greater degree of restorative crosslinking (e.g., Fig. 4C) (see Fig. S20 for extended data). Mechanical recovery across all hold times was quantified by comparing the strain energy density, $\Psi = \int_0^{0.5} T \partial \epsilon$ (i.e., the amount of work needed to strain the rafts to 50%), for the first (Ψ_1) and second (Ψ_2) cycles, where T and ϵ are the engineering stress and strain, respectively. Fig. 4D reveals that rafts re-loaded without healing ($t_h = 0$ s), exhibit decreases in strain energy from cycles 1 to 2 on the order of $\sim 30\%$, regardless of loading rate. In contrast, when recovered for 300s the strain energies of rafts loaded at 2% s⁻¹ and 4% s⁻¹ decreased by only 1.5% and 11%, respectively, with the former change being statistically insignificant (see Fig. S21 for extended data).

These measurable changes in the rafts' resistances to deformation could be indicative of adaptations in the stiffness of their underlying ant-to-ant connections, but this is not supported by differences in the characteristic shapes or moduli of the stress responses (from cycles 1 to 2). Therefore, it is more likely indicative of evolution in the attached bond concentration. Specifically, greater restoration of mechanical properties at longer hold times provides strong evidence that attachment rates and crosslink concentrations increase when initial raft densities are restored. Indeed, we observed visible instances in which voids that formed during the first loading cycle were mended by the start of the second (Fig \P C). Nevertheless, damage analysis (using identical methods to those applied in the previous section), proved too insensitive to elucidate statistically significant differences in averaged void areas or counts across recovery times (see Figs. S22-S24 and Movies S11-S12). Therefore, to extrapolate predictions about bond kinetics during recovery periods we examine the hysteresis ratio, defined as $H_{ratio} = \Psi_2/\Psi_1$, where Ψ_1 and Ψ_2 are the total strain energies of cycles 1 and 2, respectively.

Lamont et al. (2021) [17] demonstrated that for networks with constant kinetic attachment and detachment rates (k_a and k_d , respectively), H_{ratio} should recover with a characteristic healing time $\tau_h = (\bar{k}_a + \bar{k}_d)^{-1}$. Therefore, assuming that the kinetics of detachment and attachment are relatively constant during recovery, we expect this quantity to vary with the hold time t_h as:

$$H_{ratio} = 1 - \Delta \Psi^* \exp(-t_h/\tau_H), \tag{1}$$

where $\Delta \Psi^* = (\Psi_2 - \Psi_1)/\Psi_1$ is the fractional reduction in strain energy from cycles 1 to 2 when recovery time is $t_h = 0$ s. Fig. Φ E provides the experimentally-measured H_{ratio} (discrete data) alongside the best fits from Π (dashed curves).

Fig. 4D reveals that the average strain energy of cycle 1 in rafts loaded at 2% s⁻¹ is statistically lower than that for rafts loaded at 4% s⁻¹, which is consistent with the strain rate-driven stiffening observed in the first section. While this was expected, we also observed a complete recovery in rafts loaded at the slower rate when $t_h = 300$ s, but not in rafts loaded at faster rates – a surprising finding since the level of network damage is indistinguishable for the two strain rates (Figs. S22-S24). Indeed, fitting (1) to the experimental data (dashed curves in Fig. 4E) reveals that the characteristic heal time of the rafts loaded at 2 and 4% s⁻¹ are approximately 180 and 300s, respectively. This observation may be understood by considering that the heal time τ_h scales with both associative and dissociative bond kinetics. Thus, these

results suggest that the higher loading rate induces a reduction in k_a , k_d , or both, and that this effect persists during the hold times between cycles, indicating strain-rate memory. Supposing that k_a depends only on the local concentration of ants (so that it is constant during all recovery stages), the increase in healing time for quickly loaded specimens provides secondary evidence of catch bond kinetics, whereby k_d increases with strain rate. Such a behaviorally driven reduction of k_d during loading would temporarily reduce the exchange rate that otherwise promotes healing during recovery times.

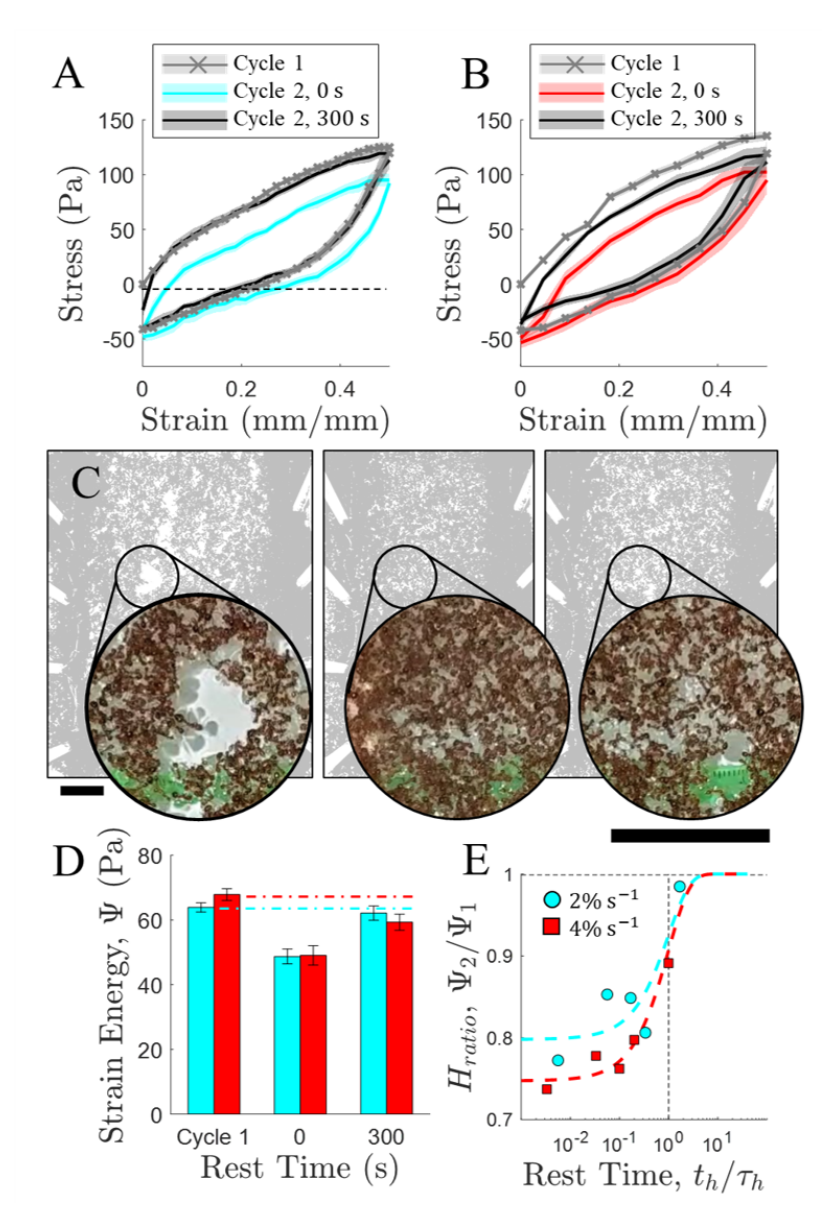


Figure 4: (A-B) Ensemble-averaged (n = 4) engineering stress versus strain (to 50%) over two loading cycles with recovery times of $t_h \in \{0,300\}$ s for strain rates of (A) 2% s⁻¹ and (B) 4% s⁻¹. See Fig. S20 for extended data across hold times. Results from the first loading cycle (grey curve with ×-shaped markers) are ensemble-averaged for all experiments (n=20) since these have identical loading conditions. Results from the second loading cycles (solid curves) are ensemble averaged only across experiments of the same recovery time (n = 4). (A-B) Shaded regions indicate S.E. (C) Close-up photos of a raft loaded at a strain rate of 4% s⁻¹ near the end of the first loading cycle (left), near the end of a 300s recovery time (center), and shortly after the start of the second loading cycle (right), exemplify the self-healing process. Full-network grey scale photos of the raft are provided in the background for spatial context (with the loading direction oriented horizontally). The scale bars on the left and right represent 10ℓ for the full-network background images and close-ups, respectively. (D) Ensemble-averaged strain energy, Ψ , for the extreme hold times of $t_h = \{0, 300\}$ s for the slower (cyan bars) and faster (red bars) strain rates. Error bars represent S.E. See Fig. S21 for the total strain energy, Ψ , stored energy (during unloading), Ψ_{el} , and dissipated energy, \mathcal{D} , at all hold times. (E) Hysteresis ratio, Ψ_2/Ψ_1 , with respect to recovery time, t/τ_h , from experiments (discrete data) and an analytical fit (dashed curves) for the slower (cyan) and faster (red) loading rates.

Conclusion

We here loaded planar fire ant rafts under uniaxial extension at various loading rates. We found that the mechanical properties of 2D rafts are in sharp contrast to the rate-dependent, shear-thinning properties of confined 3D aggregates in rheological experiments [36, 43]. While the latter were influenced by confinementinduced, non-bonded interactions (as evidenced by the similarity between properties of living and dead ants [36]), the 2D planar rafts and network models investigated here allowed us to isolate the mechanical and topological effects of solely ant-to-ant bonds. Ant rafts are soft structures and are unable to remain cohered via the weak capillary effects reported by Ko, et al. (2022) 14 at moderate strains. While we observed measurable, albeit small, strain rate-dependence for peak stresses and initial tangent moduli, we found no significant correlation between mechanical toughness or rupture strains and the investigated strain rates. Significantly, despite a weak rate-dependent stress response, void-dominated damage patterns induced failure even in the slow loading regime where Transient Network Theory [42], combined with the measured rates of unloaded bond dynamics, predict steady-state creep onset. This damage-prone response is attributed to a combination of force-induced bond stabilization (i.e., catch bond response) and the weak raft cohesion. Meanwhile, the small degree of rate-dependence observed is attributed to measurable differences in conformational relaxation (without major network restructuring) as detected through PIV analysis.

To further elucidate any rate-dependence in dissociation kinetics, we analyzed the damage characteristics of rafts via custom image analysis and found that lag strain between the peak number and area of voids is predominantly governed by the stretch of the network, rather than the duration of elapsed time. This implies that the underlying bond rupture events driving void coalescence depend more on finite bond extensibility than voluntary ant detachment events, providing further evidence of catch bonds. Nevertheless, stochastic dissociation events should not be discounted and it is possible that loading rafts at even slower rates would allow bond exchange-enabled viscous creep. However, in our previous work, we observed that ants exit the structural layer and enter the freely active top layer at a rate of $\delta \approx 0.33$ mHz [49, 46]. Given the boundary conditions applied here, we find that this culminates in dissolution of the ant rafts over hour-long timescales $(1/\delta = 1/0.33 \text{ mHz}^{-1} \approx 0.84 \text{ hrs})$ as if by some effective surface tension (Fig. S4). This rendered mechanical loading of coherent rafts at rates slower than $2\% \text{ s}^{-1}$ difficult.

To corroborate that planar ant concentration modulates bond association kinetics (because of the finite reach of ants), we loaded rafts uniaxially to 50% strain for two consecutive cycles, with various hold times between them. Significantly, rafts demonstrate restoration of mechanical properties between the first and second loading cycle, verifying their concentration-dependent self-healing. Furthermore, rafts exhibited significantly better mechanical recovery for the longest hold times ($t_h = 300$ s) than without recovery ($t_h = 0$ s). We further found a sizeable increase in heal time (180s versus 300s) for the rafts loaded at faster rates, which not only supports the notion that fire ants decrease their characteristic bond exchange times (implicating catch bonds), but also demonstrates that their altered bond kinetics persist even during the recovery time (after mechanical stress is removed). This perhaps showcases ants' capacity for complex mechanical memory as active, living constituents, which we will explore further in future work.

Materials and methods

Estimating unperturbed bond dynamic rates

To estimate the nominal ant-to-ant bond dissociation, \bar{k}_d^0 , and association, \bar{k}_a^0 , rates, top view footage of an unloaded ant raft residing between two substrates (one of which was floating and could freely articulate) was used to individually measure the attached, τ_a , and detached, τ_d , bond lifetimes of image-tracked legs using ImageJ [29]. Plotting the probability distribution functions of τ_a and τ_d , we find that they each approximate a Poisson's process [45] and that the probabilities of finding a leg at a given attached or detached lifetime respectively evolve according to $P_d = \exp(-\bar{k}_d^0 \tau_a)$ and $P_a = \exp(-\bar{k}_a^0 \tau_d)$ (Fig. S1).

Notably, mandible-involving bonding modes were not commonly observed as in the case of 3D aggregations [11].

Experimental apparatus and setup

Fig. S2 depicts a model of the apparatus used to conduct tensile testing on ant rafts. The entire apparatus was suspended above a container of water such that only the bases of the substrates to which the ants adhered (Substrates 1 and 2), as well as the base of a tertiary substrate (Substrate 3) used to estimate force were submerged below the water line. Tensile strain was applied at a controllable engineering strain rate using a belt-driven linear actuator. The top of Substrate 1 was affixed to the moving plate of the linear actuator such that the entirety of Substrate 1 translated as the linear actuator was driven. A T-shaped wooden block was rigidly affixed to one end of the linear actuator. Substrate 2 was suspended from this block via three hinges that allowed it to pivot slightly. The tops of Substrates 1 and 2 were rigidly attached to their submerged bases via five acrylic rods. These rods were each coated with PTFE and talcum powder to prevent ants from climbing the apparatus and escaping the water.

At the base of Substrates 1 and 2, Velcro was wrapped around all five rods such that the ants could easily envelop and adhere to it. Thus, the ants could form a continuous raft suspended between the two substrates. Once Substrate 1 began translating, the ants underwent uniaxial tension. To estimate force during loading, a spring was suspended underwater between the backside of Substrate 2, and the wooden bock fixed to the linear actuator track (Substrate 3). Top views of the ant rafts Fig. S2.C) were captured during loading via a camera positioned as shown in Fig. S2.B. This footage was synced up with side-view footage of the underwater spring (Fig. S2.D). Force carried by the ants was estimated by visually measuring the horizontal component of spring stretch (see **Materials and Methods** section titled, *Force Estimation*, Fig. S3 and Movie S3). Notably, the spring's elongation (and thus the displacement of Substrate 2) was on the order of 10^{-4} - 10^{-3} m, while the overall raft displacement was on the order of 10^{-1} m such that spring deflection had negligible effect on the overall raft strain during loading. Similarly, the angle of deflection of Substrate 2 was on the order of just 1° such that the change in z-axis position of Substrate 2 (and the ants attached to it) was less than 10^{-4} m.

Ant collection and mechanical testing

Fire ant workers were collected from seven separate colonies in Keller, TX. Samples were prepared from one of the randomly selected colonies by slowly flooding the container in which they were housed until the ants surfaced for collection. Once isolated from debris, the ants were massed in a tared petri dish and allowed to rest for 30 minutes before being placed into the water between the Substrates 1 and 2 of the apparatus (Fig. S2). Sample masses were consistently on the order of 10 g, indicating that there were $\sim 10^4$ ants available for each raft based on an estimated ant mass of 1 mg [18, 49, 40]. Sample shape was achieved by placing the ants in the water between Substrates 1 and 2 of the apparatus, and then gently coaxing the rafts towards each substrate before carefully cropping the excess raft material from the sides using forceps. Based on planar density estimates ($\rho \approx 0.304 \text{ ants mm}^{-2}$) of ant rafts from prior work [49] we estimate that approximately 6,000 ants comprised the structural network of each sample after cropping based on sample dimensions of $\sim 100 \times 200 \text{ mm}^{-2}$. Once in the correct shape, the rafts were allowed to rest for 10-minutes prior to testing. To ensure that differences in results were not due to colony selection, once a raft sample was set up, experiments were carried out at all reported strain rates (and/or hold times in the case of cyclic loading) before returning the ants to their habitats. To mitigate and control for any effects of cumulative ant exhaustion, the rafts were allowed to rest and self-heal at least 5-minutes between experiments. Additionally, the order of applied strain rates and hold times (for cyclic loading) was randomly assigned for each testing batch. No sample of ants was tested for more than 10 experiments before being returned to their habitat for overnight recovery.

Force estimation

Forces transmitted by the ant rafts were estimated by measuring the strain of an elastomeric spring (Fig. S2.D and Movie S3.B) of measured force-strain relation (Fig. S3). Spring strain was taken as $\epsilon = (|\mathbf{r}| - |\mathbf{r}_0|)/|\mathbf{r}_0|$ where $|\mathbf{r}|$ and $|\mathbf{r}_0|$ are the current and reference (force-free) lengths of the spring, respectively, both of which were measured using a combination of manual binary image thresholding in ImageJ [29] and automated image-analysis in MATLAB R2022b. While the spring was oriented slightly out of the horizontal plane (by angle θ), only the horizontal component of tensile strain, $\epsilon_1 = \epsilon \cos \theta$, resisting elongation of the ant raft was used to estimate resistance force and stress.

Strain rate selection

Although rafts strained at rates on the order of 0.3% s⁻¹ could be reasonably tested, we encountered that rafts loaded at rates slower than this (e.g., $\sim 0.01 - 0.1\%$ s⁻¹) were often subject to dissolution caused by the structural layer's perpetual contraction [49] and ants' preferential aggregation on the dry substrates rather than back into the structural raft network (Fig. S4). Meanwhile, systems loaded at rates greater than 6% s⁻¹ often delaminated at the ant-to-substrate interface, perhaps due to a combination of viscous drag from the water's surface and sudden onset of high local stress due to geometric stress risers at the junction. Either way, this delamination obfuscated trends in rate-dependent response (see Fig. S5 for extended mechanical response data) for loading rates > 6% s⁻¹ and so data from such rates is not reported in Figs. The Note that while drag may have induced delamination, it is ruled out as a major source of uncertainty for the reasons discussed in **SI Section S1**.

Conformational PIV Image Analysis

To characterize and corroborate the presence of rate-dependent conformational changes in the ant rafts, PIV was utilized to obtain Eulerian vector fields of the structural layers during deformation using the application, PIVlab [37], in MATLAB 2022b. Image stacks were extracted from raw footage such that the applied elongation between frames was 1 mm (roughly one-third an ant length, $\ell/3$), regardless of strain rate. This allowed for use of consistent PIV settings across strain rates. To attain sufficient spatial sampling, the interrogation length was set to $\sim \ell/3$. A dynamic mask was applied to exclude voids (defined as regions where the vacant area exceeded areal reach, $A_r = \pi \ell^2$) from the regions of interest as they nucleated. The result was a spatiotemporally resolved, instantaneous velocity field, v, at all positions, x, on the structural raft (see Figs. S7 for example). To reduce visual noise and highlight regions where ants in the raft are moving more or less synchronously with their immediate neighbors, the normalized order parameter was computed as a function of position, x, according to:

$$\varphi(x) = \frac{\int_{\Omega} v(x)}{\int_{\Omega} |v(x)|},$$
(2)

where |v| is local raft speed and the integral is carried out over a moving areal window of $\Omega = 3\ell \times 3\ell$ (or $\sim 10\% \times 10\%$ of the initial sample length, $\sim 34\ell$). The order parameter is unity wherever the ants are moving unidirectionally within the domain, Ω , and approaches zero when the motion is completely isotropic and disordered. The norm of φ is shown as a vector field in Figs. S7-S11 and Movies S4-S6 to illustrate the direction of local movement.

Ultimately, we wished to determine the local displacement everywhere on the raft with the intention to characterize the extent of local deviation in the raft from expected or *affine* behavior [25]. First, we considered the velocity field induced by the applied elongation. The velocity gradient applied at the boundaries is:

$$L_{app} = \operatorname{diag}(0, \dot{\varepsilon}(t)) \tag{3}$$

where $\dot{\varepsilon}$ is the applied strain rate in direction e_2 . Due to the non-normal camera perspective, $\dot{\varepsilon}$ was computed along the width of each sample (i.e., along direction e_1), using a discrete difference approximation

$$\dot{\varepsilon} \approx x_2(t)^{-1} \left[x_2(t+\delta t) - x_2(t) \right] / \delta t, \tag{4}$$

where x_2 is the position of each point (in the direction transverse to loading, e_2) along the moving boundary of the raft's region of interest and δt is the time between adjacent frames. Had the network followed L_{app} affinely, then the *applied* velocity could be taken as the linearly interpolated velocity between the two boundaries. This interpolation was conducted using L_{app} as follows:

$$\mathbf{v}_{app}(\mathbf{x},t) = \mathbf{L}_{app}(t)\mathbf{x}(t). \tag{5}$$

Deviation from the applied velocity field (see Fig. S8 and Movie S4 for sample heat maps) is then defined as:

$$\delta \mathbf{v} = \mathbf{v}_{app}(\mathbf{x}, t) - \mathbf{v}(\mathbf{x}, t). \tag{6}$$

We additionally decompose the velocity gradient into symmetric and skew-symmetric components to characterize local raft expansion/compression and spin (in both directions) through $tr(\mathbf{D})$, and ω_{12} , respectively. See Figs. S9-S10 and Movies S5-S6 for sample heat maps of local divergence and spin. Here, \mathbf{D} is the rate of deformation tensor, \mathbf{D} , defined as:

$$D = \frac{1}{2} (L + L^T), \tag{7}$$

while ω is the spin tensor:

$$\boldsymbol{\omega} = \frac{1}{2} (\boldsymbol{L} - \boldsymbol{L}^T). \tag{8}$$

Note that $tr(\mathbf{D})$ defines the true volumetric strain rate while $\boldsymbol{\omega}$ defines the network vorticity rate. For a discussion and visual summary of interpreted PIV results, see **SI Section S2** and Fig. S11, respectively. For extended raw data of the measures taken from (6)–(8), see Figs. S12-S15).

Damage-based image analysis

Image analysis was conducted on rafts loaded uniaxially to failure (Fig. S16-S19 and Movies S8-S10), as well as cyclically (Figs. S22-S24 and Movies S11-S12), to characterize their damage signatures (e.g., void onset and nucleation). First, colored images stacks were converted to binary using a manually adjusted color threshold in ImageJ [29], such that white pixels depicted ants, while black pixels depicted the apparatus, surrounding water, and the vacant spaces between ants. Once binary image stacks were obtained, further analysis was conducted using MATLAB R2022b. First, the four corners of the ant rafts (Fig. S16 – red dots) – defining the domains in which image analysis would be conducted – were manually identified at the initial frame of mechanical loading. To account for non-normal camera alignment and perspective, an initial linear mapping was first applied that enforced an orthonormal basis of the boundaries (see basis $\{e_1, e_2\}$ in Fig. S16.A). To then track the domain boundaries through time, the deformation gradient, $F(t) = \text{diag}(1, \epsilon(t))$, applied during mechanical loading was used to update the domains' four corners in each subsequent frame (Fig. S16 – red dotted lines).

Once bounded, the quantities, positions (i.e., centroids denoted with cyan asterisks in Fig. S16), and areal distributions of voids within the domains were measured in time. Voids are here defined as defects in the raft that are too large for an ant to reach across or traverse, and which therefore cannot be immediately mended by either surface ants depositing into them, or raft ants binding with each other from opposite sides. Thus, two image processing steps were conducted to filter out voids that did not meet these size criteria. First, white pixels were dilated by a linear distance of $\ell/2$ such that any void with a gap dimension less than the body length of a single ant would be closed. This ensured that any gaps and fissures across which ants could walk or reach were filtered out. The white pixels were then eroded by the same length to restore the remaining voids to approximately their initial areas. Second, any voids whose areas, A_v , were less than the approximate reach, $A_r \approx \pi \ell^2$, enveloped by a single ant of length, ℓ , were removed. This ensured that any voids that could be mended or closed by the deposition or positioning of a single ant, were also filtered out.

The numbers, N_v , and average normalized areas, A_v/A_r , of voids were measured. Each of these values was then ensemble-averaged over n=4 experiments. The characteristic lag strain and time (ϵ_c and τ_c) between when the peak number and area of voids occurred was then computed using the cross-correlational function between N_v and A_v , defined as:

$$G(N_v^*, A_v^*) = \langle N_v^*(\epsilon) \cdot A_v^*(\epsilon + \delta \epsilon) \rangle - \langle N_v^*(\epsilon) \rangle \langle A_v^*(\epsilon + \delta \epsilon) \rangle, \tag{9}$$

where the operator $\langle \Box \rangle$ denotes the ensemble average over data within the strain range $\epsilon \in [\delta \epsilon, \epsilon_{max} - \delta \epsilon]$ (given maximum strain, ϵ_{max}), and $\delta \epsilon$ is the incremental strain over which correlation is computed (see Fig. S19 for examples of G with respect to $\delta \epsilon$).

In addition to measuring and characterizing the void statistics, this binary image analysis was used to coarsely estimate the overall void fractions, ϕ_v , and minimum cross-sectional lengths, L, of continuous ants spanning direction e_1 (e.g., solid red lines in Figs. S16 and S22). The former value, ϕ_v , was simply taken as the ratio of black (non-ant containing) to white (ant-containing) pixels. To estimate raft cross-sectional length, L, the raft domains were partitioned into a discrete set of pixel columns parallel to the loading direction, e_1 , and spaced approximately every 1ℓ body lengths (e.g., dotted red lines in Fig. S22). The column hosting the minimum number, N_w , of white pixels was then used to loosely estimate the instantaneous minimum cross-sectional length as $L \approx N_w dx/dp$, where dp/dx is the unit conversion of pixels per unit length. However, neither ϕ_v nor L varied statistically with strain rate or between loading cycles (see Figs. S217.A-D and S23-S24.C-D, respectively).

Numerical network model

The modeled networks contain on the order of $\sim 6 \times 10^3$ simulated fire ants initiated with a planar packing fraction of 0.304 ants/mm² [49], 46], where each ant is comprised of five rigidly attached beads that replicate the morphometric aspect ratio, ~ 4 , of real ants [40]. Every ant is capable of forming up to six dynamic bonds with neighboring ants that represent the real leg-to-leg bonds. Each bond is prescribed a divergent, nonlinear force-displacement relation according to the potential energy:

$$U_b(r) = \varepsilon_b \frac{r^2}{(r_c^2 - r^2)},\tag{10}$$

where r is the length of the bond, ε_b is an energy scale (whose increase stiffens the bonds and visa versa), and r_c is the bond length at which force diverges. This nonlinear bond potential was selected based on the notion that during deformation, ant-to-and bonds (e.g. legs) must first undergo softer unfolding before stretching to their full length, upon which the material comprising the bonds themselves must deform. This likely causes stiffening akin to that of polymer chains stretched near their full contour lengths [17]. Moreover, we were unable to reproduce the high degrees of strain localization and void formation observed experimentally when using linear springs.

No finite rest length is prescribed for bonds through (10), as we observed that structural ants in rafts continually contracted in our prior work [49]. Instead, to prevent network collapse (due to tensile bond forces), all ants also impart soft repulsive forces on nearest neighbors that mimic volume exclusion effects, according to the energy potential:

$$U_r(d) = f_r^0 \kappa \exp(-d/\kappa), \tag{11}$$

where d is the distance between two beads, f_r^0 is the repulsive force at zero separation (set finitely for numerical stability but sufficiently high to prevent beads from passing through one another), and κ is a length scale set to $\ell/5$ so that repulsive forces were approximately zero at a pairwise separation distance of one ant body length (specifically, $f_r(\ell) < 1\% f_r^0$). We found that setting $f_r^0 = 0.1\varepsilon_b/\kappa$ consistently reproduced the correct initial raft dimensions while maintaining numerical stability for all values of ε_b explored.

To mimic bond dynamics, the leg-to-leg bonds can stochastically break and reform without damage. This is achieved by prescribing a discrete probability of a bond event occurring during each discrete timestep (δt) according to:

$$\delta P = 1 - \exp(k_i \delta t),\tag{12}$$

where k represents either the constant attachment or detachment rate (k_a and k_d , respectively), and we have assumed Markovian processes [45] so that current events are uncorrelated with prior events [47]. For the initial set of simulations, k_a and k_d were prescribed at the experimentally measured rates (in unperturbed rafts) of $\bar{k}_a^0 = 84.8$ mHz and $\bar{k}_d^0 = 7.4$ mHz, respectively. These rates correspond to an average steady-state coordination number of $z = \bar{k}_a^0/(\bar{k}_a^0 + \bar{k}_d^0)z_m \approx 5.5$, where $z_m = 6$ is the maximum number of connections per ant in the simulation. Foster, et al. (2014) [11] estimated that the coordination number in 3D fire ant aggregations is approximately $z_{3D} \approx 14$ bonds per ant. Supposing that the 2D planar coordination number scales as $z_{2D} \approx (z_{3D})^{3/2} = 5.8$, then our models' coordination numbers approximate realistic values. For every simulation, rafts were always equilibrated (i.e., brought to steady state) by allowing stochastic attachment and detachment at rates \bar{k}_a^0 and \bar{k}_d^0 , respectively. However, during deformation, k_d was swept over $k_d/\bar{k}_d^0 = \{0, 0.01, 0.1, 1\}$ and we found that results predicted using lower values of k_d (e.g., $k_d/\bar{k}_d^0 = 0.01$ in Fig. [2] and $k_d = 0$ in Fig. [3]) more closely mirrored experimental observations. While the stochastic or voluntary detachment rate, k_d , was sometimes set to or near zero during deformation, bond detachment was still always enforced when the force, f_b , in a bond exceeded $f_{max} = 200$ dynes (based on the estimations of Phonekeo, et al. (2016) [23]), which accounts for the finite extensibility of ant legs.

The boundary conditions on the simulated domains were such that the top and bottom 5% of the ants in the raft, representing the ants adhered to the substrates in real experiments, were spatially fixed during initial equilibration and then displaced using the prescribed strain rate of $\dot{\epsilon} = 2\%$ s⁻¹ during loading. The positions of all other (non-displacement boundary) ants were updated based on their unbalanced forces, $\mathbf{f}^{\alpha} = \sum_{\beta} \nabla_{\mathbf{r}} U(\mathbf{r}^{\alpha\beta})$ using a velocity-Verlet algorithm, where $\mathbf{r}^{\alpha\beta}$ is the end-to-end vector between bead α and its β^{th} interacting neighbor, and $U = U_r + U_b$ is the total energy potential governed by (10) and (11). Boundary displacement and bond kinetics (via (12)) were applied at discrete time intervals of δt . However, to enforce the conditions of quasi-static force balance without overdamping, 40,000 iterations of positional integration were conducted between every timestep.

The repulsion length scale ($\kappa = \ell/5$), maximum bond force ($f_{max} = 200$ dynes), and attachment rate ($k_a = 84.8$ mHz) were all held constant. The detachment rate, k_d , was swept as described above. Thus, the only remaining free parameters were ε_b and r_c . Rather than sweep ε_b directly, we found it useful to consider the bond length, r_{max} , at which bond rupture occurs (i.e., where $\partial U_b/\partial r = f_{max}$ through (10)). Thus we defined a dimensionless ratio, $\chi = r_{max}/r_c$, through which ε_b was set based on f_{max} , r_c , and χ according to:

$$\varepsilon_b = \frac{f_{max}r_c}{2\chi}(1-\chi^2)^2. \tag{13}$$

See Fig. S25 for a plot of bond force, $f_b = \partial U_b/\partial r$, versus length, r, that denotes f_{max} , r_{max} , and r_c when χ is swept over three values. The force divergence length, r_c , and ratio, χ , were swept over the ranges $r_c/\ell \in [1.1, 1.4]$ and $\chi \in [0.7, 0.8]$, respectively. We found that setting $r_c/\ell = 1.3$ and $\chi = 0.74$ reasonably minimized the mean absolute error between numerical and experimental stresses, average void areas, and void counts (Fig. S26).

Estimating ideal toughness and strength

According to Lake and Thomas $\boxed{16}$, the toughness Γ_0 of a network scales with mesh size ξ , number of load-carrying constitutents per unit volume c and the energy stored in a single unit at rupture U_b according to:

$$\Gamma_0 = c\xi U_b. \tag{14}$$

As noted in the main text, we take the mesh size, ξ , of our network to be $\xi \approx \rho^{-1/2} = 1.8$ mm based on the experimentally measured planar packing density of ants. Furthermore, we assume a raft thickness

of the width of one ant, $w \approx 1$ mm, and coordination number of roughly z = 5.5 based on the model so that $c = \frac{\rho z}{2w} \approx 0.85$ bonds mm⁻³, where the factor of 1/2 is included since every bond is shared by two ants. Based on the values of ε_b and r_c that minimized mean absolute error between our discrete model and experiments ($\varepsilon_b = 1.05 \ \mu\text{J}$ and $r_c = 3.8$ mm, respectively), the energy stored in a bond at rupture (through (10)) is $U_b = 1.275 \times 10^{-6}$ J so that the estimated toughness is $\Gamma_0 \approx 1.96$ Pa. Similarly to toughness, ultimate strength of an ideal network may be estimated as $T = c\xi f_{max}$ where the bond energy at break has simply been replaced by the estimated bond rupture force estimate. Taking the rupture force as that of a leg-to-leg bond (195 ± 7 dynes (23)) provides a strength estimate of $T = 2.99 \pm 0.11$ kPa, while instead conservatively estimating rupture force as that of weaker leg-to-body bonds (69 ± 52 dynes (23)) yields $T = 1.06 \pm 0.80$ kPa. The lowest range assuming all leg-to-body bonds with strengths at the 16th percentile produces a strength estimate of T = 260 Pa where actual estimates are on the order of 100 Pa (Fig. (10)).

Acknowledgement

F.J.V. gratefully acknowledges the support of the National Science Foundation (NSF) under award no. 1761918. This content is solely the responsibility of the authors and does not necessarily represent the official views of NSF.

F.J.V. and S.C.L. acknowledge support by the Department of Energy, National Nuclear Security Administration, Predictive Science Academic Alliance Program (PSAAP) under Award Number DE-NA0003962. This report was prepared as an account of work sponsored by an agency of the United States Government. Neither the United States Government nor any agency thereof, nor any of their employees, makes any warranty, express or implied, or assumes any legal liability or responsibility for the accuracy, completeness, or usefulness of any information, apparatus, product, or process disclosed, or represents that its use would not infringe privately owned rights. Reference herein to any specific commercial product, process, or service by trade name, trademark, manufacturer, or otherwise does not necessarily constitute or imply its endorsement, recommendation, or favoring by the United States Government or any agency thereof. The views and opinions of authors expressed herein do not necessarily state or reflect those of the United States Government or any agency thereof.

S.C.L would like to thank Joel Clemmer and Dan Bolintineanu for their support in algorithmic development.

References

- [1] Benjamin J Adams et al. "Raft formation by the red imported fire ant, Solenopsis invicta". In: Journal of Insect Science 11.1 (Jan. 2011), p. 171. ISSN: 1536-2442. DOI: 10.1673/031.011.17101. URL: https://doi.org/10.1673/031.011.17101 (visited on 05/24/2023).
- [2] Visar Ajeti et al. "Wound healing coordinates actin architectures to regulate mechanical work". en. In: Nature Physics 15.7 (July 2019). Publisher: Nature Publishing Group, pp. 696-705. ISSN: 1745-2481. DOI: 10.1038/s41567-019-0485-9. URL: https://www.nature.com/articles/s41567-019-0485-9 (visited on 01/22/2021).
- [3] Christopher W. Barney et al. "Cavitation in soft matter". In: Proceedings of the National Academy of Sciences 117.17 (Apr. 2020). Publisher: Proceedings of the National Academy of Sciences, pp. 9157–9165. DOI: 10.1073/pnas.1920168117. URL: https://www.pnas.org/doi/10.1073/pnas.1920168117 (visited on 08/13/2023).
- [4] Werner Brandt. "Calculation of Compressibilities of High Polymers from the Energy of Interaction between Chain Groups". In: *The Journal of Chemical Physics* 26.2 (Oct. 2004), pp. 262–270. ISSN: 0021-9606. DOI: 10.1063/1.1743282. URL: https://doi.org/10.1063/1.1743282 (visited on 05/25/2023).

- [5] Hongyi Cai et al. "Highly stretchable ionically crosslinked acrylate elastomers inspired by polyelectrolyte complexes". en. In: Soft Matter 18.39 (Oct. 2022). Publisher: The Royal Society of Chemistry, pp. 7679–7688. ISSN: 1744-6848. DOI: 10.1039/D2SM00755J. URL: https://pubs.rsc.org/en/content/articlelanding/2022/sm/d2sm00755j (visited on 05/19/2023).
- [6] Yunjing Chen et al. "Disentanglement induced by uniaxial pre-stretching as a key factor for toughening poly(l-lactic acid) sheets". en. In: *Polymer* 140 (Mar. 2018), pp. 47–55. ISSN: 0032-3861. DOI: 10.1016/j.polymer.2018.02.032. URL: https://www.sciencedirect.com/science/article/pii/S0032386118301563 (visited on 08/13/2023).
- [7] A. Deblais, S. Woutersen, and D. Bonn. "Rheology of Entangled Active Polymer-Like T. Tubifex Worms". In: *Physical Review Letters* 124.18 (May 2020). Publisher: American Physical Society, p. 188002. DOI: 10.1103/PhysRevLett.124.188002. URL: https://link.aps.org/doi/10.1103/PhysRevLett.124.188002 (visited on 02/05/2023).
- [8] Gregory T. Dee and Bryan B. Sauer. "The cohesive energy density of polymers and its relationship to surface tension, bulk thermodynamic properties, and chain structure". en. In: Journal of Applied Polymer Science 134.5 (2017). _eprint: https://onlinelibrary.wiley.com/doi/pdf/10.1002/app.44431. ISSN: 1097-4628. DOI: [10.1002/app.44431]. URL: https://onlinelibrary.wiley.com/doi/abs/10.1002/app.44431] (visited on 08/09/2023).
- [9] Nicolas Desprat et al. "Creep Function of a Single Living Cell". en. In: Biophysical Journal 88.3 (Mar. 2005), pp. 2224-2233. ISSN: 0006-3495. DOI: 10.1529/biophysj.104.050278. URL: https://www.sciencedirect.com/science/article/pii/S0006349505732823 (visited on 05/25/2023).
- [10] Etienne Ducrot et al. "Toughening Elastomers with Sacrificial Bonds and Watching Them Break". en. In: Science 344.6180 (Apr. 2014). Publisher: American Association for the Advancement of Science, pp. 186–189. ISSN: 0036-8075, 1095-9203. DOI: 10.1126/science.1248494. URL: https://science.sciencemag.org/content/344/6180/186 (visited on 06/08/2021).
- [11] Paul C. Foster et al. "Fire ants actively control spacing and orientation within self-assemblages". en. In: Journal of Experimental Biology 217.12 (June 2014). Publisher: The Company of Biologists Ltd, pp. 2089–2100. ISSN: 0022-0949, 1477-9145. DOI: 10.1242/jeb.093021. URL: https://jeb.biologists.org/content/217/12/2089 (visited on 11/08/2020).
- [12] Justin P. Gallivan and Dennis A. Dougherty. "Cation- interactions in structural biology". In: Proceedings of the National Academy of Sciences 96.17 (Aug. 1999). Publisher: Proceedings of the National Academy of Sciences, pp. 9459–9464. DOI: 10.1073/pnas.96.17.9459. URL: https://www.pnas.org/doi/10.1073/pnas.96.17.9459 (visited on 05/24/2023).
- [13] D.L. Hu et al. "Entangled active matter: From cells to ants". en. In: *The European Physical Journal Special Topics* 225.4 (July 2016), pp. 629-649. ISSN: 1951-6401. DOI: 10.1140/epjst/e2015-50264-4. URL: https://doi.org/10.1140/epjst/e2015-50264-4 (visited on 02/05/2023).
- [14] Hungtang Ko, Ting-Ying Yu, and David L. Hu. "Fire ant rafts elongate under fluid flows". en. In: Bioinspiration & Biomimetics 17.4 (June 2022). Publisher: IOP Publishing, p. 045007. ISSN: 1748-3190. DOI: 10.1088/1748-3190/ac6d98. URL: https://dx.doi.org/10.1088/1748-3190/ac6d98 (visited on 02/05/2023).
- [15] Hungtang Ko et al. "Small fire ant rafts are unstable". In: Physical Review Fluids 7.9 (Sept. 2022). Publisher: American Physical Society, p. 090501. DOI: 10.1103/PhysRevFluids.7.090501. URL: https://link.aps.org/doi/10.1103/PhysRevFluids.7.090501 (visited on 02/05/2023).
- [16] G. J. Lake, A. G. Thomas, and David Tabor. "The strength of highly elastic materials". In: Proceedings of the Royal Society of London. Series A. Mathematical and Physical Sciences 300.1460 (Aug. 1967). Publisher: Royal Society, pp. 108–119. DOI: 10.1098/rspa.1967.0160. URL: https://royalsocietypublishing.org/doi/10.1098/rspa.1967.0160 (visited on 12/31/2020).

- [17] Samuel C. Lamont et al. "Rate-Dependent Damage Mechanics of Polymer Networks with Reversible Bonds". In: *Macromolecules* 54.23 (Dec. 2021). Publisher: American Chemical Society, pp. 10801–10813. ISSN: 0024-9297. DOI: 10.1021/acs.macromol.1c01943. URL: https://doi.org/10.1021/acs.macromol.1c01943 (visited on 02/05/2023).
- [18] Nathan J. Mlot, Craig A. Tovey, and David L. Hu. "Fire ants self-assemble into waterproof rafts to survive floods". In: Proceedings of the National Academy of Sciences 108.19 (May 2011). Publisher: Proceedings of the National Academy of Sciences, pp. 7669-7673. DOI: 10.1073/pnas.1016658108. URL: https://www.pnas.org/doi/10.1073/pnas.1016658108 (visited on 05/24/2023).
- [19] Thierry Mora et al. "Local equilibrium in bird flocks". In: *Nature physics* 12.12 (2016), pp. 1153–1157.
- [20] Jason Mulderrig, Brandon Talamini, and Nikolaos Bouklas. "A statistical mechanics framework for polymer chain scission, based on the concepts of distorted bond potential and asymptotic matching". en. In: Journal of the Mechanics and Physics of Solids 174 (May 2023), p. 105244. ISSN: 0022-5096.

 DOI: 10.1016/j.jmps.2023.105244. URL: https://www.sciencedirect.com/science/article/pii/S0022509623000480 (visited on 05/25/2023).
- [21] Gary K. Nave et al. "Attraction, Dynamics, and Phase Transitions in Fire Ant Tower-Building". In: Frontiers in Robotics and AI 7 (2020). ISSN: 2296-9144. URL: https://www.frontiersin.org/articles/10.3389/frobt.2020.00025 (visited on 08/26/2023).
- [22] O. Peleg et al. "Collective mechanical adaptation of honeybee swarms". en. In: Nature Physics 14.12 (Dec. 2018). Publisher: Nature Publishing Group, pp. 1193–1198. ISSN: 1745-2481. DOI: 10.1038/s41567-018-0262-1. URL: https://www.nature.com/articles/s41567-018-0262-1 (visited on 05/24/2023).
- [23] Sulisay Phonekeo et al. "Ant aggregations self-heal to compensate for the Ringelmann effect". en. In: Soft Matter 12.18 (May 2016). Publisher: The Royal Society of Chemistry, pp. 4214–4220. ISSN: 1744-6848. DOI: 10.1039/C6SM00063K. URL: https://pubs.rsc.org/en/content/articlelanding/2016/sm/c6sm00063k. (visited on 02/03/2021).
- [24] Sulisay Phonekeo et al. "Fire ants perpetually rebuild sinking towers". In: Royal Society Open Science 4.7 (July 2017). Publisher: Royal Society, p. 170475. DOI: 10.1098/rsos.170475. URL: https://royalsocietypublishing.org/doi/10.1098/rsos.170475 (visited on 02/05/2023).
- [25] R. C. Picu. "Mechanics of random fiber networks—a review". en. In: Soft Matter 7.15 (July 2011). Publisher: The Royal Society of Chemistry, pp. 6768-6785. ISSN: 1744-6848. DOI: 10.1039/C1SM05022B. URL: https://pubs.rsc.org/en/content/articlelanding/2011/sm/c1sm05022b (visited on 07/19/2023).
- [26] Robert H. Pullen and Steven M. Abel. "Catch Bonds at T Cell Interfaces: Impact of Surface Reorganization and Membrane Fluctuations". eng. In: *Biophysical Journal* 113.1 (July 2017), pp. 120–131. ISSN: 1542-0086. DOI: [10.1016/j.bpj.2017.05.023].
- [27] Sergio A. Rincon et al. "Kinesin-5-independent mitotic spindle assembly requires the antiparallel microtubule crosslinker Ase1 in fission yeast". en. In: *Nature Communications* 8.1 (May 2017). Publisher: Nature Publishing Group, p. 15286. ISSN: 2041-1723. DOI: 10.1038/ncomms15286. URL: https://www.nature.com/articles/ncomms15286 (visited on 01/07/2021).
- [28] Michael Rubinstein and Ralph H. Colby. *Polymer Physics*. en. Hardcover Michael Rubinstein; Ralph H. Colby -. Cc: ir Lang: en Tab: overview. Oxford University Press, June 2003. (Visited on 10/05/2021).
- [29] Caroline A. Schneider, Wayne S. Rasband, and Kevin W. Eliceiri. "NIH Image to ImageJ: 25 years of image analysis". en. In: *Nature Methods* 9.7 (July 2012). Publisher: Nature Publishing Group, pp. 671–675. ISSN: 1548-7105. DOI: 10.1038/nmeth.2089. URL: https://www.nature.com/articles/nmeth.2089 (visited on 07/20/2023).

- [30] I. Slavkov et al. "Morphogenesis in robot swarms". In: Science Robotics 3.25 (Dec. 2018). Publisher: American Association for the Advancement of Science, eaau9178. DOI: 10.1126/scirobotics.aau9178. URL: https://www.science.org/doi/full/10.1126/scirobotics.aau9178 (visited on 08/09/2023).
- [31] Evgeni V. Sokurenko, Viola Vogel, and Wendy E. Thomas. "Catch bond mechanism of force-enhanced adhesion: counter-intuitive, elusive but ... widespread?" In: Cell host & microbe 4.4 (Oct. 2008), pp. 314–323. ISSN: 1931-3128. DOI: 10.1016/j.chom.2008.09.005. URL: https://www.ncbi.nlm.nih.gov/pmc/articles/PMC2610669/ (visited on 11/16/2020).
- [32] Evgeny B. Stukalin et al. "Self-Healing of Unentangled Polymer Networks with Reversible Bonds". In: *Macromolecules* 46.18 (Sept. 2013). Publisher: American Chemical Society, pp. 7525–7541. ISSN: 0024-9297. DOI: 10.1021/ma401111n. URL: https://doi.org/10.1021/ma401111n (visited on 01/08/2021).
- [33] Alan Pasha Tabatabai et al. "Detailed Balance Broken by Catch Bond Kinetics Enables Mechanical-Adaptation in Active Materials". en. In: Advanced Functional Materials 31.10 (2021). _eprint: https://onlinelibrar p. 2006745. ISSN: 1616-3028. DOI: 10.1002/adfm.202006745. URL: https://onlinelibrary.wiley.com/doi/abs/10.1002/adfm.202006745 (visited on 04/28/2022).
- [34] Cihan Tekoğlu, JW Hutchinson, and Thomas Pardoen. "On localization and void coalescence as a precursor to ductile fracture". In: *Philosophical Transactions of the Royal Society A: Mathematical, Physical and Engineering Sciences* 373.2038 (2015), p. 20140121.
- [35] Michael Tennenbaum and Alberto Fernandez-Nieves. "Activity effects on the nonlinear mechanical properties of fire-ant aggregations". In: *Physical Review E* 102.1 (July 2020). Publisher: American Physical Society, p. 012602. DOI: 10.1103/PhysRevE.102.012602. URL: https://link.aps.org/doi/10.1103/PhysRevE.102.012602 (visited on 11/04/2020).
- [36] Michael Tennenbaum et al. "Mechanics of fire ant aggregations". en. In: Nature Materials 15.1 (Jan. 2016). Number: 1, pp. 54–59. ISSN: 1476-4660. DOI: 10.1038/nmat4450. URL: https://www.nature.com/articles/nmat4450 (visited on 05/24/2023).
- [37] William Thielicke and René Sonntag. "Particle Image Velocimetry for MATLAB: Accuracy and enhanced algorithms in PIVlab". en-US. In: Journal of Open Research Software 9.1 (May 2021). Number: 1, p. 12. ISSN: 2049-9647. DOI: 10.5334/jors.334. URL: https://openresearchsoftware.metajnl.com/articles/10.5334/jors.334 (visited on 05/24/2023).
- [38] Wendy E. Thomas, Viola Vogel, and Evgeni Sokurenko. "Biophysics of Catch Bonds". In: *Annual Review of Biophysics* 37.1 (2008). _eprint: https://doi.org/10.1146/annurev.biophys.37.032807.125804, pp. 399-416. DOI: 10.1146/annurev.biophys.37.032807.125804. URL: https://doi.org/10.1146/annurev.biophys.37.032807.125804. (visited on 07/19/2023).
- [39] Ruiping Tong et al. "Highly Stretchable and Compressible Cellulose Ionic Hydrogels for Flexible Strain Sensors". In: *Biomacromolecules* 20.5 (May 2019). Publisher: American Chemical Society, pp. 2096–2104. ISSN: 1525-7797. DOI: 10.1021/acs.biomac.9b00322. URL: https://doi.org/10.1021/acs.biomac.9b00322 (visited on 01/07/2021).
- [40] Walter R. Tschinkel. "The Morphometry of Solenopsis Fire Ants". en. In: *PLOS ONE* 8.11 (Nov. 2013). Publisher: Public Library of Science, e79559. ISSN: 1932-6203. DOI: 10.1371/journal.pone. 0079559. URL: https://journals.plos.org/plosone/article?id=10.1371/journal.pone. 0079559 (visited on 05/25/2023).
- [41] Hiroyuki Tsukeshiba et al. "Effect of Polymer Entanglement on the Toughening of Double Network Hydrogels". In: *The Journal of Physical Chemistry B* 109.34 (Sept. 2005). Publisher: American Chemical Society, pp. 16304–16309. ISSN: 1520-6106. DOI: 10.1021/jp052419n. URL: https://doi.org/10.1021/jp052419n (visited on 08/13/2023).

- [42] Franck J. Vernerey, Rong Long, and Roberto Brighenti. "A statistically-based continuum theory for polymers with transient networks". In: Journal of the Mechanics and Physics of Solids 107 (Oct. 2017), pp. 1–20. ISSN: 0022-5096. DOI: 10.1016/j.jmps.2017.05.016. URL: http://www.sciencedirect.com/science/article/pii/S0022509617301874 (visited on 11/21/2018).
- [43] Franck J. Vernerey et al. "How do fire ants control the rheology of their aggregations? A statistical mechanics approach". eng. In: *Journal of the Royal Society, Interface* 15.147 (2018). ISSN: 1742-5662. DOI: 10.1098/rsif.2018.0642.
- [44] Tamás Vicsek and Anna Zafeiris. "Collective motion". en. In: *Physics Reports*. Collective motion 517.3 (Aug. 2012), pp. 71–140. ISSN: 0370-1573. DOI: 10.1016/j.physrep.2012.03.004. URL: https://www.sciencedirect.com/science/article/pii/S0370157312000968 (visited on 05/24/2023).
- [45] Robert J. Wagner, Ethan Hobbs, and Franck J. Vernerey. "A network model of transient polymers: exploring the micromechanics of nonlinear viscoelasticity". en. In: Soft Matter 17.38 (Oct. 2021). Publisher: The Royal Society of Chemistry, pp. 8742–8757. ISSN: 1744-6848. DOI: 10.1039/D1SM00753J. URL: https://pubs.rsc.org/en/content/articlelanding/2021/sm/d1sm00753j (visited on 05/19/2023).
- [46] Robert J. Wagner and Franck J. Vernerey. "Computational exploration of treadmilling and protrusion growth observed in fire ant rafts". en. In: *PLOS Computational Biology* 18.2 (Feb. 2022). Publisher: Public Library of Science, e1009869. ISSN: 1553-7358. DOI: 10.1371/journal.pcbi.1009869. URL: https://journals.plos.org/ploscompbiol/article?id=10.1371/journal.pcbi.1009869 (visited on 05/19/2023).
- [47] Robert J. Wagner and Franck J. Vernerey. "Coupled bond dynamics alters relaxation in polymers with multiple intrinsic dissociation rates". en. In: Soft Matter 19.15 (Apr. 2023). Publisher: The Royal Society of Chemistry, pp. 2716–2725. ISSN: 1744-6848. DOI: 10.1039/D3SM00014A. URL: https://pubs.rsc.org/en/content/articlelanding/2023/sm/d3sm00014a (visited on 05/25/2023).
- [48] Robert J. Wagner et al. "A mesoscale model for the micromechanical study of gels". en. In: Journal of the Mechanics and Physics of Solids 167 (Oct. 2022), p. 104982. ISSN: 0022-5096. DOI: 10. 1016/j.jmps.2022.104982. URL: https://www.sciencedirect.com/science/article/pii/S0022509622001740 (visited on 05/19/2023).
- [49] Robert J. Wagner et al. "Treadmilling and dynamic protrusions in fire ant rafts". In: Journal of The Royal Society Interface 18.179 (June 2021). Publisher: Royal Society, p. 20210213. DOI: 10.1098/rsif.2021.0213. URL: https://royalsocietypublishing.org/doi/10.1098/rsif.2021.0213 (visited on 05/19/2023).
- [50] Lin Xu et al. "Thermosensitive P(AAc-co-NIPAm) Hydrogels Display Enhanced Toughness and Self-Healing via Ion-Ligand Interactions". en. In: *Macromolecular Rapid Communications* 43.19 (2022). _eprint: https://onlinelibrary.wiley.com/doi/pdf/10.1002/marc.202200320, p. 2200320. ISSN: 1521-3927. DOI: 10.1002/marc.202200320. URL: https://onlinelibrary.wiley.com/doi/abs/10.1002/marc.202200320 (visited on 05/19/2023).
- [51] Canhui Yang, Tenghao Yin, and Zhigang Suo. "Polyacrylamide hydrogels. I. Network imperfection". en. In: Journal of the Mechanics and Physics of Solids 131 (Oct. 2019), pp. 43–55. ISSN: 0022-5096.

 DOI: 10.1016/j.jmps.2019.06.018. URL: https://www.sciencedirect.com/science/article/pii/S0022509619302200 (visited on 05/03/2023).
- [52] Frank W. Zok. "Integrating lattice materials science into the traditional processing-structure-properties paradigm". en. In: MRS Communications 9.4 (Dec. 2019), pp. 1284–1291. ISSN: 2159-6867. DOI: 10.1557/mrc.2019.152. URL: https://doi.org/10.1557/mrc.2019.152 (visited on 08/13/2023).